Additively manufactured biodegradable porous iron

Li, Yageng; Jahr, H.; Lietaert, K.; Pavanram, P.; Yilmaz, A.; Fockaert, L. I.; Leeflang, M. A.; Pouran, B.; Gonzalez-Garcia, Y.; Weinans, H.

DOI
10.1016/j.actbio.2018.07.011

Publication date
2018

Document Version
Final published version

Published in
Acta Biomaterialia

Citation (APA)
Li, Y., Jahr, H., Lietaert, K., Pavanram, P., Yilmaz, A., Fockaert, L. I., Leeflang, M. A., Pouran, B., Gonzalez-Garcia, Y., Weinans, H., Mol, J. M. C., Zhou, J., & Zadpoor, A. A. (2018). Additively manufactured biodegradable porous iron. *Acta Biomaterialia*, *77*, 380-393. https://doi.org/10.1016/j.actbio.2018.07.011

Acta Biomaterialia 77 (2018) 380–393

Contents lists available at ScienceDirect

Acta Biomaterialia

journal homepage: www.elsevier.com/locate/actabiomat

Full length article

Additively manufactured biodegradable porous iron

Y. Li [a,*], H. Jahr [b,c], K. Lietaert [d,e], P. Pavanram [b], A. Yilmaz [f], L.I. Fockaert [f], M.A. Leeflang [a], B. Pouran [a,g], Y. Gonzalez-Garcia [f], H. Weinans [a,g,h], J.M.C. Mol [f], J. Zhou [a,1], A.A. Zadpoor [a,1]

[a] Department of Biomechanical Engineering, Delft University of Technology, Delft 2628 CD, The Netherlands
[b] Department of Anatomy and Cell Biology, University Hospital RWTH Aachen, Aachen 52074, Germany
[c] Department of Orthopedic Surgery, Maastricht UMC+, Maastricht 6202 AZ, The Netherlands
[d] 3D Systems – LayerWise NV, Grauwmeer 14, Leuven 3001, Belgium
[e] KU Leuven Department of Materials Engineering, Kasteelpark Arenberg 44, Leuven 3001, Belgium
[f] Department of Materials Science and Engineering, Delft University of Technology, Delft 2628 CD, The Netherlands
[g] Department of Orthopedics, UMC Utrecht, Heidelberglaan 100, Utrecht 3584CX, The Netherlands
[h] Department of Rheumatology, University Medical Center Utrecht, Utrecht 3584CX, The Netherlands

ARTICLE INFO

Article history:
Received 7 May 2018
Received in revised form 14 June 2018
Accepted 5 July 2018
Available online 6 July 2018

Keywords:
Additive manufacturing
Direct metal printing
Iron scaffolds
Biodegradation
Mechanical property
Biocompatibility

ABSTRACT

Additively manufactured (AM) topologically ordered porous metallic biomaterials with the proper biodegradation profile offer a unique combination of properties ideal for bone regeneration. These include a fully interconnected porous structure, bone-mimicking mechanical properties, and the possibility of fully regenerating bony defects. Most of such biomaterials are, however, based on magnesium and, thus, degrade too fast. Here, we present the first report on topologically ordered porous iron made by Direct Metal Printing (DMP). The topological design was based on a repetitive diamond unit cell. We conducted a comprehensive study on the *in vitro* biodegradation behavior (up to 28 days), electrochemical performance, time-dependent mechanical properties, and biocompatibility of the scaffolds. The mechanical properties of AM porous iron (E = 1600–1800 MPa) were still within the range of the values reported for trabecular bone after 28 days of biodegradation. Electrochemical tests showed up to ≈12 times higher rates of biodegradation for AM porous iron as compared to that of cold-rolled (CR) iron, while only 3.1% of weight loss was measured after 4 weeks of immersion tests. The biodegradation mechanisms were found to be topology-dependent and different between the periphery and central parts of the scaffolds. While direct contact between MG-63 cells and scaffolds revealed substantial and almost instant cytotoxicity in static cell culture, as compared to Ti-6Al-4V, the cytocompatibility according to ISO 10993 was reasonable in *in vitro* assays for up to 72 h. This study shows how DMP could be used to increase the surface area and decrease the grain sizes of topologically ordered porous metallic biomaterials made from metals that are usually considered to degrade too slowly (e.g., iron), opening up many new opportunities for the development of biodegradable metallic biomaterials.

Statement of Significance

Biodegradation in general and proper biodegradation profile in particular are perhaps the most important requirements that additively manufactured (AM) topologically ordered porous metallic biomaterials should offer in order to become the ideal biomaterial for bone regeneration. Currently, most biodegradable metallic biomaterials are based on magnesium, which degrade fast with gas generation. Here, we present the first report on topologically ordered porous iron made by Direct Metal Printing (DMP). We also conducted a comprehensive study on the biodegradation behavior, electrochemical performance, biocompatibility, and the time evolution of the mechanical properties of the implants. We show that these implants possess bone-mimicking mechanical properties, accelerated degradation rate, and reasonable cytocompatibility, opening up many new opportunities for the development of iron-based biodegradable materials.

* Corresponding author.
E-mail address: y.li-7@tudelft.nl (Y. Li).
[1] Authors contributed equally to the study.

https://doi.org/10.1016/j.actbio.2018.07.011
1742-7061/

1. Introduction

Additively manufactured (AM) porous metallic biomaterials have recently emerged as promising bone substitutes with unprecedented opportunities for improving bone regeneration [1,2]. The topological design of AM porous biomaterials can be precisely controlled and customized [3], which can then be exploited to mimic the mechanical properties of bone [4], accommodate cell proliferation and differentiation, and eventually enhance bone regeneration [5]. To date, the vast majority of the AM metallic porous biomaterials have been made from bio-inert materials such as titanium alloys [6–8], pure titanium [9], stainless steel [10], tantalum [11], nitinol [7], and cobalt-chromium [12]. The main limitation of these bio-inert materials is that they stay permanently in the body as foreign objects, which may lead to permanent physical irritation and chronic local inflammatory reactions [13]. As a consequence, there may be a need for a second surgery. Even when no additional surgery is required, bone regeneration may not be complete [14]. Biodegradability is therefore considered to be an equally important requirement for an ideal bone substitute.

Biodegradable metals have recently gained much attention due to their attractive degradation characteristics and high mechanical properties as compared to those of biodegradable polymers and ceramics [15]. Among biodegradable metals, those based on magnesium and iron have been studied the most [16–25]. The important challenge when dealing with magnesium-based biomaterials is that their degradation rates are relatively high [15,26]. On the contrary, the major disadvantage for iron-based materials is their slow degradation rates [27]. AM porous metallic biomaterials generally have much larger surface area as compared to their solid counterparts [28]. This may be not an advantage for magnesium-based materials, because larger surface area normally results in an even higher biodegradation rate. Increased surface area could, however, be an important advantage for materials that degrade too slowly such as iron and its alloys. Besides, iron-based alloys possess better mechanical properties than Mg-based alloys [29], making them more interesting as porous biomaterials.

In addition, iron is inexpensive [25] and does not release hydrogen gas during biodegradation. Moreover, a number of animal studies have reported that iron-based biomaterials exhibit good biocompatibility [27,30–32]. So far, only a few studies on the development of iron scaffolds for orthopedic applications have appeared in the literature and powder metallurgy techniques [33–35], electrodeposition [36], ink/binder-jetting [16,29], or space holder [37–40] have been used.

Here, we demonstrate for the first time how direct metal printing (DMP) could be used to fabricate topologically ordered porous iron. We also present a comprehensive study on the biodegradation behavior, electrochemical performance, biocompatibility, and the evolution of the mechanical properties of the scaffolds over time.

2. Material and methods

2.1. Scaffold manufacturing and post processing

Design files were prepared with Magics (Materialise, Belgium) and DMP Control software (3D Systems, Belgium). The samples were designed to have a height of 10.5 mm, a diameter of 10 mm, a relative density of 20%, and a diamond unit cell with a strut thickness 200 μm and a cell size of 1 mm (Fig. 1a, b). A ProX DMP 320 machine (3D Systems, Belgium) was used for sample preparation. We used a nitrogen gas atomized Fe powder (Material Technology Innovations Co., Ltd., China) (Fig. 1c) with the following characteristics: purity: 99.88%; particle sizes: D_{10} = 32 μm, D_{50} = 48 μm and D_{90} = 71 μm; morphology: spherical; apparent density: 4.09 g/cm^3; tap density: 4.88 g/cm^3; angle of repose: 157°; carbon content: 0.0044%. The microstructure (Fig. S1) of the iron powder was also analyzed. The powder was deposited in layers of 30 μm during DMP. Given the low relative density of the samples, only contour but no hatch vectors were used (Fig. 1d, 0.33 W/mm energy density). The samples were built on a steel base plate and were later on removed from this base plate with electrical discharge machining (EDM). Powder particles entrapped in pores were removed by means of ultrasonic cleaning in 96% ethanol for 20 min. Then, the samples were chemically cleaned in 50% HCl for 1 min to remove residuals from EDM and loose powder particles, followed by 5 min ultrasonic cleaning in 96% ethanol again to wash out HCl.

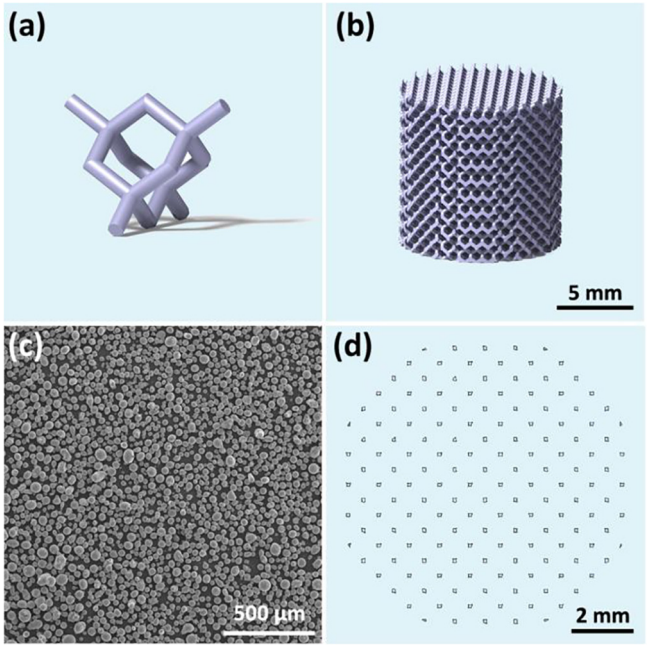

Fig. 1. Scaffold design and manufacturing: (a) diamond unit cell, (b) scaffold design, (c) Fe powder particle morphology, and (d) an example of one layer scanned in the AM process (DMP Control software).

2.2. Topological characterization

The iron scaffolds were imaged using micro-computed tomography (μCT) (Quantum FX, Perkin Elmer, USA) at a tube current of 180 μA , a tube voltage of 90 kV, a scan time of 3 min, and a resolution of (30 μm)^3 with a total 3600 projections. μCT images were automatically reconstructed and converted into a series of 2D images using Analyze 11.0 (Perkin Elmer, USA). Then, the images were exported to FIJI (NIH, Bethesda, MD, USA) and locally thresholded using Bernsen algorithm (radius = 15). This allowed accurate segmentation of the scaffolds and capturing of their morphological features. Afterwards, circular regions of interest (ROIs) with a diameter of 10 mm were created on the cross section of the scaffolds. After thresholding and using the cylindrical ROIs which overlay the total volume of the scaffolds, porosity (defined as the ratio of the void volume to the scaffold volume), averaged strut thickness (Tb.Th) and averaged strut spacing (Tb.Sp), i.e., pore size, were calculated using BoneJ (a plugin of FIJI).

2.3. Microstructural characterization

The microstructures of the as-built iron samples were examined using an optical microscope (OM, model BX60M, Olympus) after

etching by a 5% Nital reagent (5 ml HNO_3 per 100 ml C_2H_5OH). The microstructure of the as-received cold rolled (CR) Armco iron samples (AK Steel, the Netherlands) with high purity (>99.85%) was examined as a reference material. The average grain size was measured using the line intercept method.

2.4. Immersion tests

In vitro degradation tests were conducted in revised simulated body fluid [41] (r-SBF) in open beakers and the beakers were kept in a stirred thermostatic bath at 37 °C for up to 28 days. To determine weight changes, samples were taken out of the r-SBF solution, ultrasonically cleaned with 99% acetone and 96% ethanol for 30 min each, dried at room temperature, and finally weighed using a balance with an accuracy of 0.1 mg. pH values (accuracy: ±0.002, InLab Expert Pro-ISM, METTLER TOLEDO) of the medium were registered after 1, 2, 7, 14, and 28 days of *in vitro* degradation. Fe, Ca, and P ion concentrations in the solution were analyzed at different time points using an inductively coupled plasma optical emission spectroscope (ICP-OES, iCAP 6500 Duo, Thermo Scientific).

2.5. Characterization of degradation products

The morphology and composition of the degradation products on the surface of the samples after the biodegradation tests were analyzed at selected time points with a scanning electron microscope equipped with energy-dispersive X-ray spectroscopy (EDS) (SEM, JSM-IT100, JEOL). In addition to observing the periphery of the samples, we cut the samples and observed the degradation products in the center. Phase identification of the degradation products was performed using an X-ray diffractometer (XRD, Bruker D8 Advance diffractometer in Bragg-Brentano geometry). The diffractometer was equipped with a graphite monochromator and Vantec position sensitive detector and operated at 45 kV and 35 mA with a step size of 0.034° and a dwell time of 30 s per step using Co Ka radiation. In addition, Fourier-transform infrared spectroscopy (FTIR) spectra were obtained from a Thermo-Nicolet Nexus FTIR apparatus equipped with a liquid-nitrogen cooled MCT-A (mercury-cadmium-telluride) detector and a SAGA grazing angle accessory at an incident angle of 80°. An infrared background spectrum was collected on a freshly polished sample prior to the analysis of the degraded samples. The final spectra were compared against this background. For each spectrum, 128 scans at a resolution of 4 cm^{-1} were co-added.

2.6. Electrochemical tests

For electrochemical tests, AM iron samples were mounted in an epoxy resin and ground with 800 grit SiC sandpaper. The picture of the sample's cross section was imported into ImageJ and the surface area of 0.24 cm^2 exposed to electrolyte of was measured through the Analyze Particles option in ImageJ. Copper screws were placed inside the resin to make the samples conductive. Electrochemical tests were performed in a 1250/1255 Solartron potentiostat in r-SBF at 37 °C. A three-electrode electrochemical cell was set up with a platinum mesh as the counter electrode, Ag/AgCl as the reference electrode, and Fe specimen as the working electrode. Potentiodynamic polarization (PDP) was applied to test the sample after 1-day and 28-day immersion. The set-up was first stabilized for 1 h to reach the open circuit potential (OCP). Then, the polarization started at an initial potential of −0.3 V below OCP and was increased to +0.5 V above OCP at a scan rate of 0.5 mV/s. Electrochemical impedance spectroscopy (EIS) was conducted at different immersion time points (1, 2, 3, 7, 14, 21, and 28 days). The amplitude of the signal was 10 mV versus OCP over a frequency range between 100 kHz and 10 mHz for impedance data acquisition. The CR iron samples with surface area of 0.5 cm^2 (>99.85% purity, ARMCO Iron) were also analyzed as a reference material.

2.7. Mechanical characterization

Compression tests were carried out using an Instron machine with 10 kN load cell at a crosshead speed of 2 mm/min. No lubrication was applied on the compression plates. The mechanical properties of the as-built, as-polished, and as-degraded AM porous iron were determined according to ISO 13314:2011 and the quasi-elastic gradient (hereafter referred to as the elastic modulus) and yield strength were obtained. Elastic modulus of the porous material was determined as the slope of the initial linear part of the stress-strain curve using linear fitting in Origin software. The initial linear part of the stress-strain curve was offset by 0.2% and its intersection with the stress-strain curve was taken to calculate the yield strength. Stress-strain curves were obtained at different immersion time points (i.e., 1, 2, 7, 14 and 28 days). The tests were performed in triplicate per time point and the average values of the elastic modulus and yield strength were calculated.

2.8. Biocompatibility assessment

2.8.1. Extract preparation

Biocompatibility evaluation was essentially performed as described before [42]. Briefly, AM iron scaffolds were stored dry and at ambient temperature to prevent corrosion. Prior to assessing cytotoxicity, scaffolds (Ø 10 mm × 10 mm, $n = 5$) were weighed, immersed for 30 min in 100% isopropanol (Merck, Darmstadt, Germany) at room temperature, air-dried and subsequently incubated in Dulbecco's modified eagle medium (DMEM) with low glucose (Sigma) supplemented with 10% fetal calf serum (PAN Biotech) for 72 h under physiological conditions (5% CO_2, 20% O_2, 95% humidity, 37 °C). Extracts were then prepared according to EN ISO standards 10993:5 and 10993:12, respectively, with a specimen weight to extraction medium ratio of 0.2 g/mL being 1X. Less concentrated extracts (e.g., 10X) were likewise prepared using more extraction medium. In parallel, Ti-6Al-4V (ASTM Grade 5) extracts (1X) were prepared as negative controls [42]. Dimethyl sulfoxide (DMSO) (20%) was used as positive controls [43]. Prior to cytotoxicity testing, extracts were sterile filtered using a 0.2 μm syringe filter.

2.8.2. Cytotoxicity assays

For indirect cytotoxicity tests, 2,500 MG-63 cells were seeded, in technical triplicates, per well of a 96-well plate and precultured for 12 h prior to exchanging DMEM for Fe-extracts. Cell viability was then tested using MTS assay (CellTiter 96® AQueous One Solution Cell Proliferation Assay, Promega, G3580) at 0, 24, 48 and 72 h, with unconditioned DMEM as negative control. Prior to the addition of MTS tetrazolium compound, all media and extracts were replaced with fresh cell culture medium in order to prevent any interference of metal extract with the tetrazolium salt. MTS test was further performed according to manufacturer's instructions. Briefly, at respective time points, 20 μL of CellTiter 96® AQueous One Solution Reagent was pipetted into each well of the 96-well plate containing indicator cells in 100 μL of culture medium. Plates were incubated at 37 °C for 2 h and the absorbance was subsequently recorded at 490 nm. Relative cellular activity (X) was calculated using the following formula:

$$X = \frac{OD(test)}{OD(negative\ control)} \times 100\%$$

Independently, lactate dehydrogenase (LDH) release into the medium was quantified as another biomarker for cytotoxicity. Briefly, MG-63 cells were seeded as described above (see MTS assay) prior to assessing cytotoxicity using Pierce™ LDH Cytotoxicity Assay Kit (Thermo Scientific, 88954) according to the manufacturer's instructions with spontaneous LDH Activity Controls (water) and Maximum LDH Activity Controls (10X Lysis Buffer added 45 min before measurement). At respective time points, 50 μL of each sample was pipetted in replicates with 50 μL of Reaction Mixture into clean 96-well wells prior to incubation at room temperature for 30 min protected from light. Stop Solution (50 μL) was then added and absorbance was measured at 490 and 680 nm. Relative percentage of LDH activity was calculated according to the manufacturer's description.

2.8.3. Direct cytotoxicity assay

Cytotoxicity was further evaluated using live/dead staining (Live and Dead Cell Assay kit; Abcam, ab115347), as we described before [42]. Cells were analyzed using fluorescent microscopy (KEYENCE; live $Emission_{max}$ 495 nm, $Excitation_{max}$ 515 nm and dead Em_{max} 528 nm, Ext_{max} 617 nm. Per iron (Ø 10 mm × 1 mm) and titanium (Ø 15 mm × 1 mm) scaffold, 50,000 and 75,000 MG-63 cells were seeded and incubated for 1 h. Thereafter, 2 ml of fresh medium was added prior to 24 h incubation in replicates, after which live/dead staining was performed, as described above.

SEM analyses were performed, as previously described [42]. Briefly, cell-seeded scaffolds were carefully rinsed in phosphate buffered saline (1X PBS) and fixed for 1 h in 3% glutaraldehyde (Agar Scientific, Wetzlar, Germany) in 0.1 M Sorensen's phosphate buffer (Merck, Darmstadt, Germany) at room temperature, followed by 10 min dehydration steps in 30, 50, 70, 90 and 100% ethanol (last step twice). Samples were then air-dried at room temperature prior to sputter-coating (Sputter Coater EM SCD500, Leica, Wetzlar, Germany) with 12.5 nm of gold–palladium and imaged at 10 kV in SEM (ESEM XL 30 FEG, FEI, Eindhoven, The Netherlands).

Table 1
Topological characteristics of AM iron scaffolds.

AM iron scaffolds	Strut size (μm)	Pore size (μm)	Porosity
Design	200	800	80%
Micro CT	249 ± 6	749 ± 22	77.7 ± 1%
Weight	–	–	73.2 ± 0.1%

2.9. Statistical analysis

Optical density data (MTS, LDH) were normalized to respective controls and relative cytotoxicity was analyzed by two-way ANOVA ($\alpha = 0.05$) and post-hoc Tukey's multiple comparisons test ($\alpha = 0.05$) with $p < 0.0001$, ****; $p < 0.001$, ***; $p < 0.01$, **; $p < 0.05$, *; *n.s.* = not significant.

3. Results

3.1. Topological and surface characteristics of the scaffolds

The as-built scaffolds had an average strut size of 249 ± 6 μm (design value = 200 μm) and a pore size of 749 ± 22 μm (design value = 800 μm) (Table 1). The porosity of the scaffolds was 77.7 ± 1% or 73.2 ± 0.1% respectively, calculated from μCT or weighing, (Table 1). The reconstructed 3D model from μCT is shown in Fig. S2. The weighing method was based on the formula: Porosity = $1 - (W_{iron}/V_{bulk})/\rho_{iron}$, where W_{iron} is the weight of the sample, V_{bulk} the bulk volume of the scaffold and ρ_{iron} the density of pure iron. The surface of the as-built sample was relatively smooth both on the periphery (Supplementary document, Fig. S3a) and in the center (Supplementary document, Fig. S3c) of the scaffolds. After chemical polishing, a reduced number of unmelted powder particles were present on the external struts of the scaffolds (Supplementary document, Fig. S3b), while the struts in the center were less affected by chemical polishing (Supplementary document, Fig. S3d). The weight reduction after chemical polishing was 2.2% ± 0.1%.

3.2. Microstructure of the scaffolds

AM iron had much finer grains with an average size of 12 ± 6 μm (Fig. 2a) than CR iron that had an average grain size around 65 ± 22 μm (Fig. 2b). However, the gains of CR Fe iron were more regularly shaped than those of AM iron (Fig. 2).

3.3. In vitro degradation behavior of the scaffolds

Brownish degradation products appeared on the surface of the scaffolds on day 1 (Fig. 3a). From day 2 to day 28, the degradation product layer became thicker and the color became darker (Fig. 3a). After 28 days, the samples were completely covered by brownish degradation products (Fig. 3a). At day 28, the iron

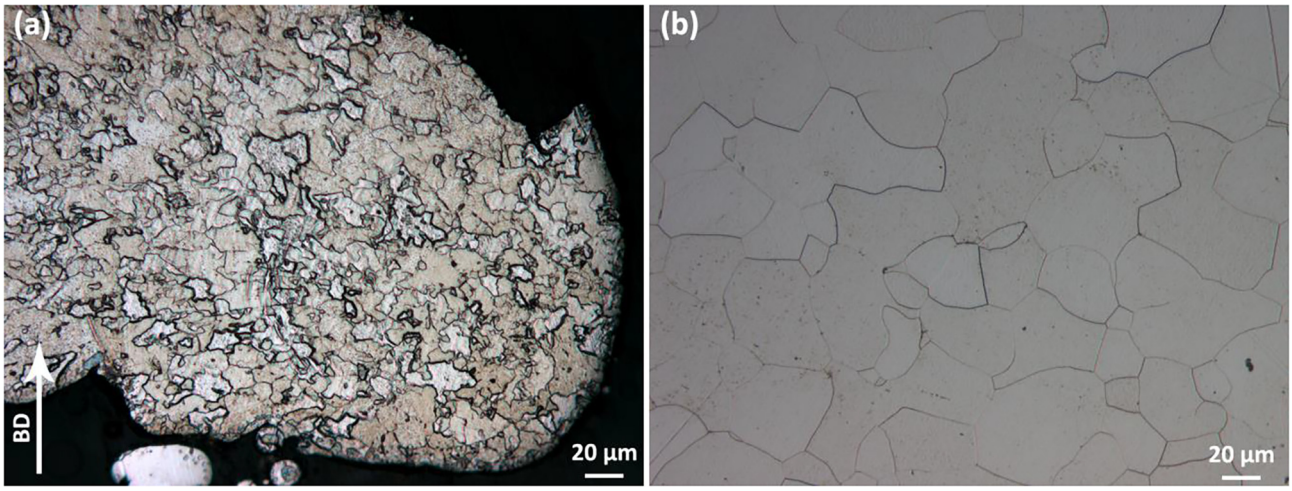

Fig. 2. Microstructures of iron samples: (a) AM porous iron and (b) CR iron.

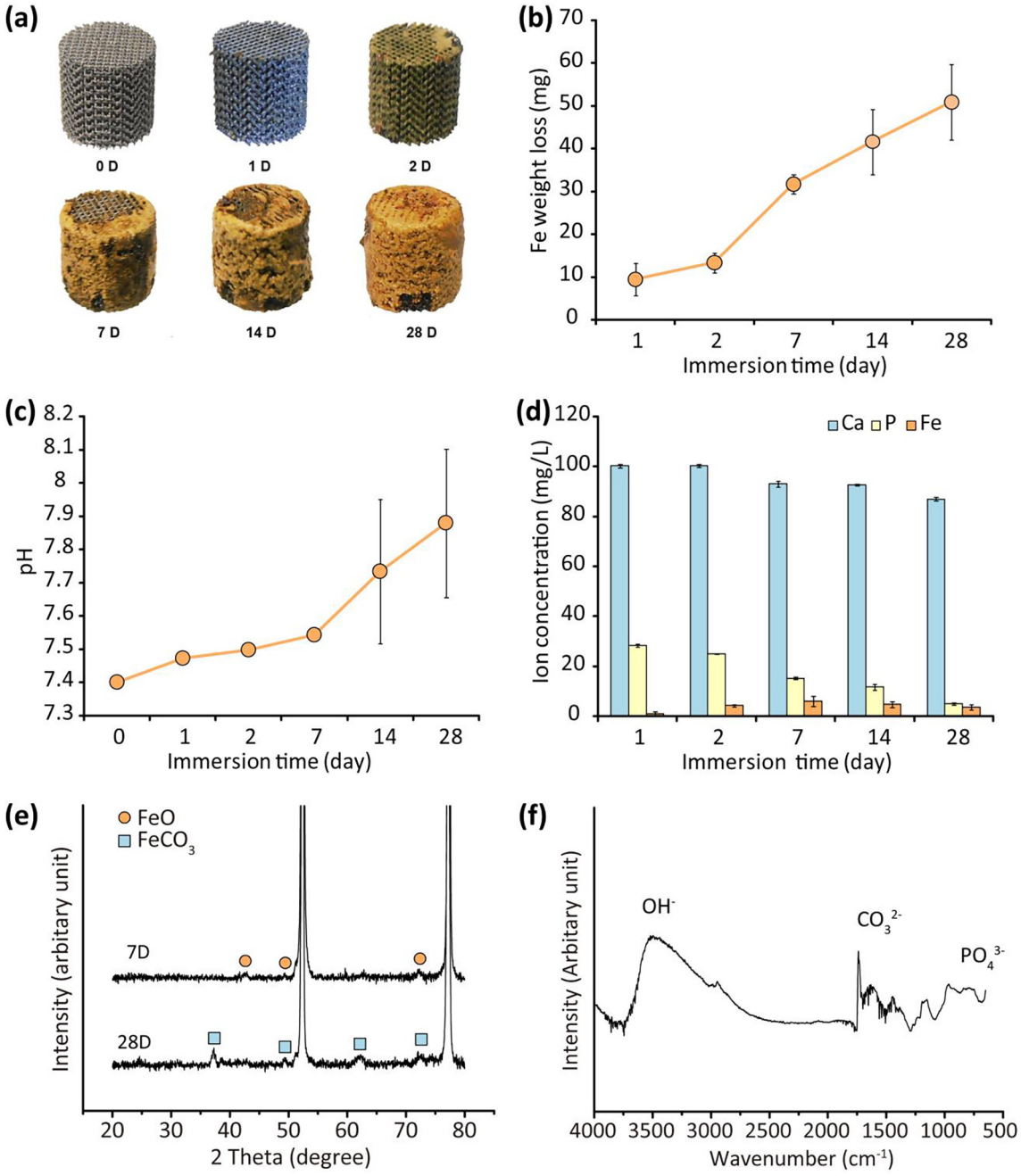

Fig. 3. *In vitro* degradation behavior of iron scaffolds: (a) visual inspection of as-degraded scaffolds, (b) weight loss, (c) pH variation with immersion (error bar invisible before day 7 because of small deviation), (d) ion concentration variation with immersion time, (e) XRD analysis and (f) FTIR analysis of degradation products.

scaffolds showed a 3.1% weight reduction (Fig. 3b) after sample cleaning. The pH values of the r-SBF solution increased from 7.4 to 7.8 after 28-day immersion (Fig. 3c). Fe ion concentration increased from 0.98 to 6.03 mg/L until day 7 (Fig. 3d) and then it started to decrease at day 14 (Fig. 3d). Ca and P ion concentrations kept decreasing during the whole immersion test period of 28 days (Fig. 3d).

3.4. Characterization of degradation products

The degradation products contained iron protoxide (FeO) and iron carbonate ($FeCO_3$) (Fig. 3e) according to XRD patterns. However, the intensity peaks of these degradation products in the XRD patterns were quite low (Fig. 3e). The FTIR spectra revealed that carbonates, hydroxides and phosphates were present in the corrosion layer (Fig. 3f) with characteristic hydroxide-specific absorption bands at about 3400 cm^{-1} [44], while the peaks at 1750 cm^{-1} and 1000 cm^{-1} likely resulted from CO_3^{2-} and PO_4^{3-} functional groups, respectively [45,46].

SEM analysis of the external struts showed that, after 1 day immersion, a thin layer of white degradation products (white in SEM and brown from visual observation) already adhered to the surface (Fig. 4a, 1 D). From day 7, groups of shiny white loose degradation products formed on the strut surface (Fig. 4a, 7 D and 14 D) while they covered almost the whole strut surface at day 28 (Fig. 4a, 28 D). Different degradation behavior was observed from center to periphery of the scaffolds (Fig. 4b). The degradation products at day 7 were thinner and more condensed at the center

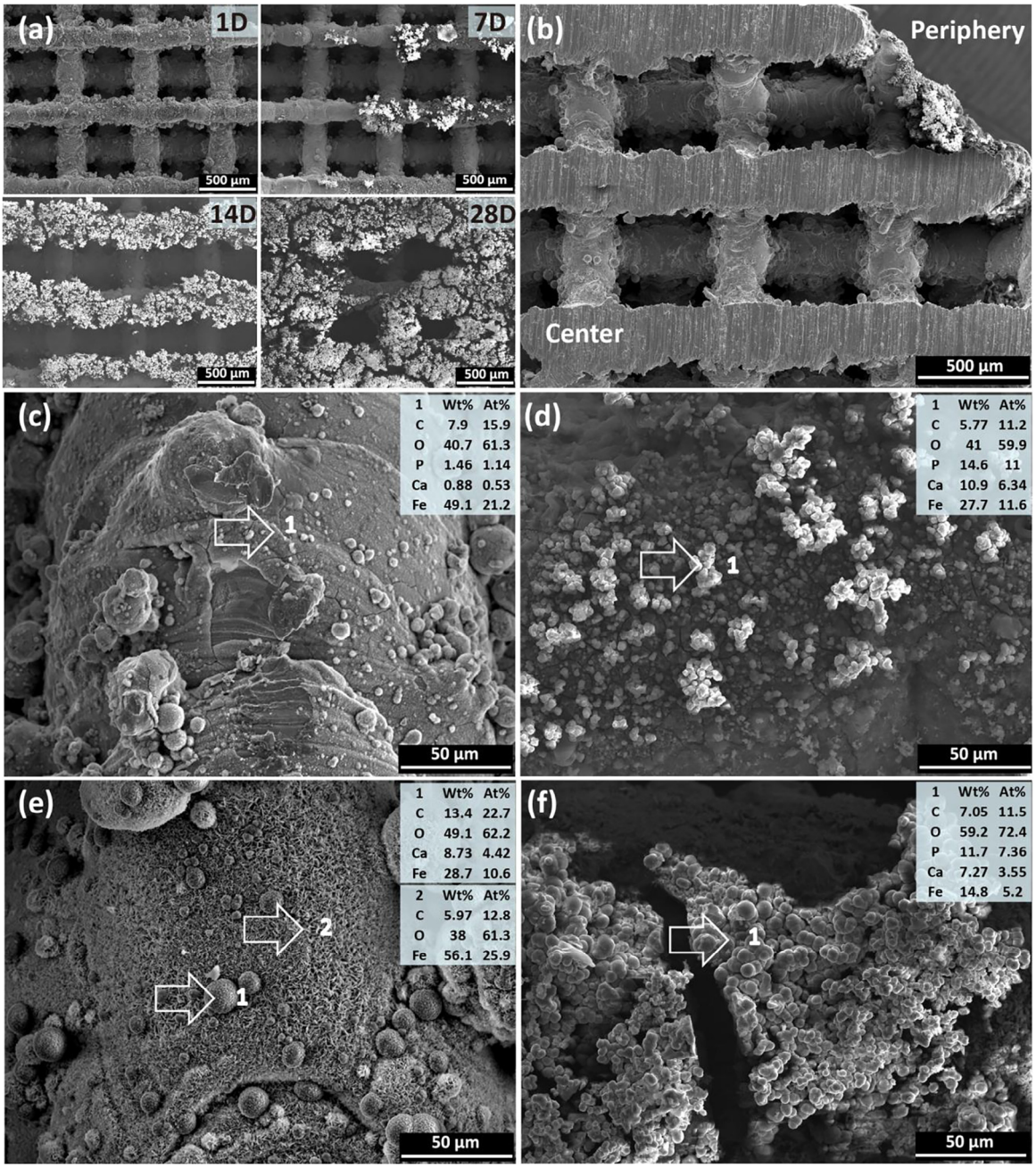

Fig. 4. SEM and EDS analyses of degradation products from the scaffold periphery to the center: (a) degradation products on the periphery at different immersion time points, (b) cross section of the scaffolds after 7-day immersion, (c) degradation products in the center and (d) on the periphery after 7-day immersion, (e) degradation products in the center and (f) on the periphery after 28-day immersion. 1 indicates the spot where EDS analysis was performed.

of the samples (Fig. 4c) while loose and thicker degradation products (Fig. 4d) were formed on the periphery. The degradation products in the center (Fig. 4c, spot 1) and on the periphery (Fig. 4d, spot 1) all contained C, O, P, Ca, and Fe, with higher P and Ca concentrations on the periphery. After 28 days of immersion, the degradation products in the center had two types of ordered crystal-like structures, one being spherically shaped and containing C, O, Ca and Fe (Fig. 4e, spot 1) and the other being feather-shaped and containing C, O and Fe only (Fig. 4e, spot 2), all without P. The morphologies of the degradation products on the periphery exhibited features similar to those observed after 7 days (Fig. 4d). The compositions were also similar to those observed after 7 days with increased O and decreased Fe concentrations (Fig. 4f, spot 1).

3.5. Electrochemical behavior

According to the potentiodynamic polarization curves, AM iron exhibited higher corrosion current densities as compared to CR iron both at day 1 and at day 28 (Fig. 5a, b), while the OCP values were similar. The corrosion current density at day 1 was 102.8 ± 19.2 $\mu A/cm^2$ and 8.6 ± 0.9 $\mu A/cm^2$ for AM iron and CR iron samples (Fig. 5a), respectively. The corrosion rates, assuming relatively uniform corrosion, calculated for AM iron and iron CR specimens according to ASTMG59 were 1.18 ± 0.22 and 0.10 ± 0.01 mm/year, respectively.

Both AM and CR samples exhibited increases in impedance modulus values at low and medium frequency from day 1 to 3,

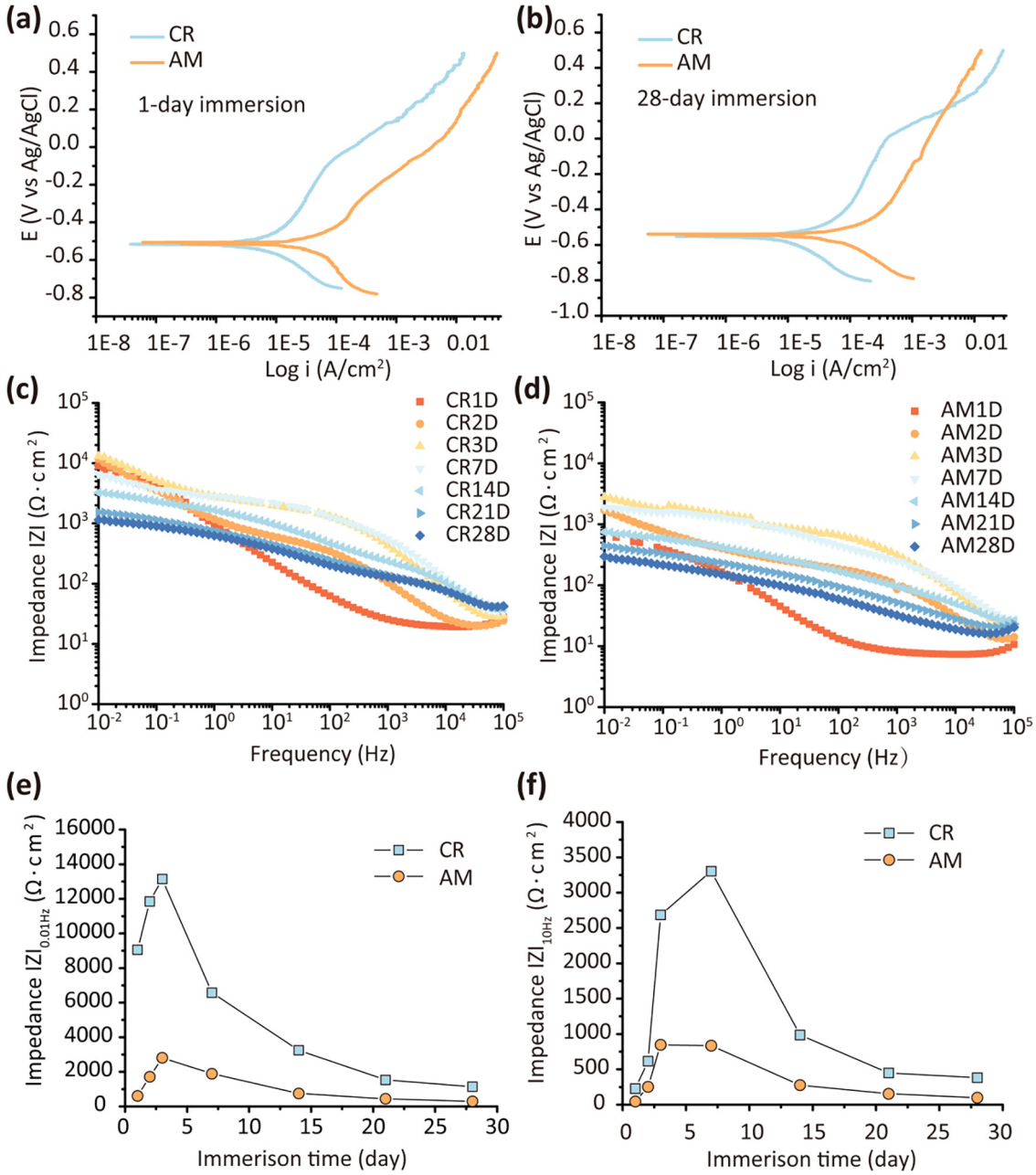

Fig. 5. Electrochemical performance of AM porous iron in comparison with CR iron: (a) PDP curves after 1-day immersion and (b) after 28-day immersion, (c), (d) Bode impedance modulus of CR iron (d) and AM porous iron (d), (e),(f) impedance modulus value at (e) low (0.01 Hz) and (f) medium (10 Hz) frequency of samples as a function of immersion time.

as observable in the Bode impedance modulus diagram (Fig. 5c, d). The impedance started decreasing from day 7 and remained decreasing up to day 28 (Fig. 5c, d). At the same immersion time points, AM iron samples always showed smaller impedance modulus values than CR iron samples at both low ($|Z|_{0.01Hz}$) and medium frequency ($|Z|_{10Hz}$) (Fig. 5e, f).

3.6. Mechanical properties

Under uniaxial compression, the as-built, as-polished, and degraded specimens without cleaning exhibited smooth stress-strain curves (Fig. 6a, b) without sudden drop. The curves all followed similar patterns with a linear elastic region at beginning and a rapidly decreased slope afterwards, followed by a plateau stage with almost no fluctuations (Fig. 6a, b). The differences in the elastic modulus and yield strength between the as-built and as-polished samples were negligible (Fig. 6a). The elastic modulus decreased after 1-day immersion, but it increased from day 2 and remained almost unchanged until day 14. Then, it decreased again at day 28 (Fig. 6c). From day 1 to day 28, the yield strength decreased gradually from 23.7 to 22.4 MPa (Fig. 6d).

3.7. Biocompatibility in vitro

Direct cytocompatibility assays (Figs. 7 and 8), employing live-dead staining and SEM, were relatively hard to quantify, although clearly only limited numbers of MG-63 appeared to survive direct exposure to iron scaffolds (Fig. 7). Of note, micrographs (Fig. 8)

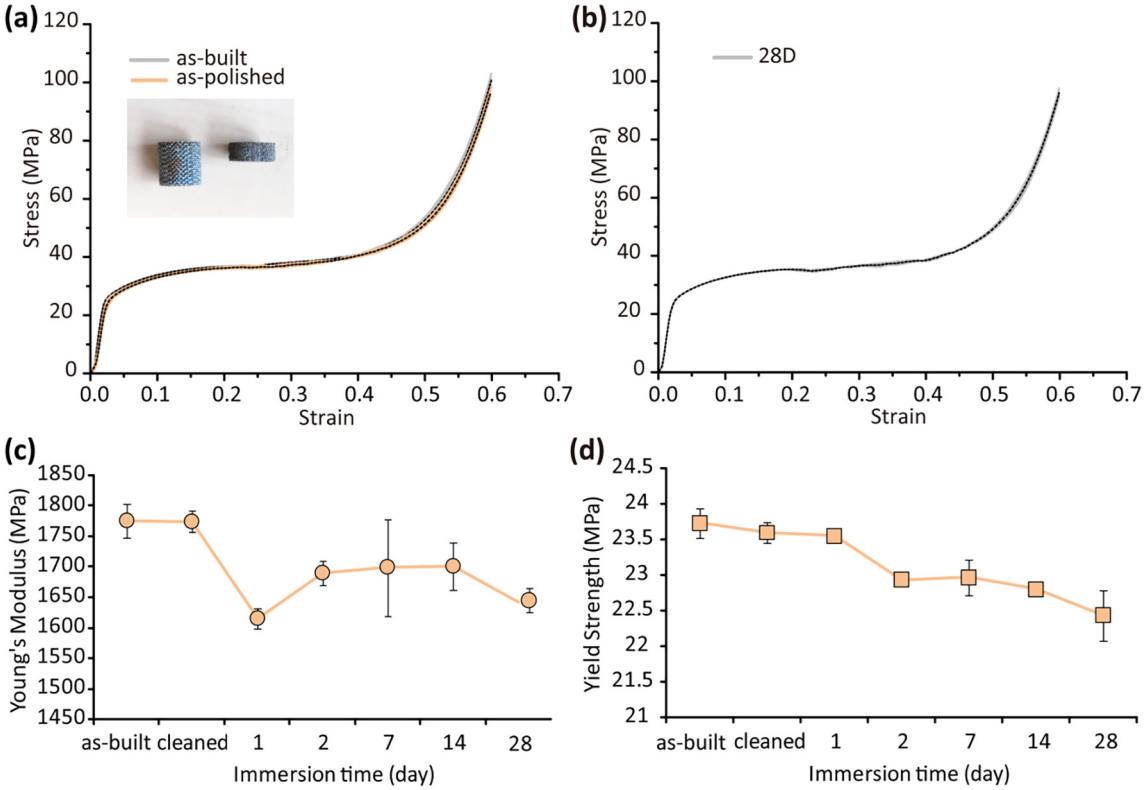

Fig. 6. Mechanical behavior: (a) compressive stress-strain curves of as-built and as-polished scaffolds (inset showing the specimen at the start and at a strain of 60%), (b) compressive stress-strain curves of porous iron after 28 day immersion, (c) elastic modulus change with immersion time and (d) yield strength change with immersion time.

revealed MG-63 cells in intimate contact to the iron scaffold. While cells developed filopodia-like protrusions on Ti-6Al-4V, a more condensed cell morphology appeared on eroded iron surface (Fig. 8d). After 24 h, viable cells (green) were hardly detectable on iron (Fig. 7), while red fluorescence from the majority of cells revealed compromised membrane integrity. Live-dead staining on Ti-6Al-4V scaffolds showed that the vast majority of cells were viable (green).

LDH assay (Fig. 9a) revealed level 0 cytotoxicity (i.e., ≤25% cell death) for Ti-6Al-4V at all time points, with the largest SD at 72 h. DMSO was 100% cytotoxic after 72-h incubation. Level 1 cytotoxicity was determined for Fe, with increasing levels of cytotoxicity with increasing extraction time, ranging from 25% after 24 h to just below 40% after 72 h. As an independent means to assess cytocompatibility, cell viability was determined using MTS assay (Fig. 9b): with Ti-6Al-4V extracts, MG-63 cells were about 100% viable independent of the extraction time, with slightly higher SD at longer time points. MG-63 cells on iron extracts revealed 75% viability at 24 h, with a decreasing trend with longer incubations; reaching 40% viability for the 72-h extraction.

4. Discussion

4.1. Microstructure

Micro melt pools formed [47] during DMP leads to high cooling rates (10^3 to 10^8 K/s) [48], which results in a non-equilibrium solidification process and enhances grain refinement. The average grain size of AM porous iron was more than 5 times smaller than that of CR iron. Moreover, unlike previously reported AM solid iron [49,50], the AM porous scaffolds had no elongated grains oriented in parallel with the building direction. This indicates that the effects of directional solidification were not as strong as in the case of solid counterparts, as the struts of the scaffolds were built in a tilted direction.

4.2. Biodegradation behavior

Based on the PDP results, AM porous iron showed higher values of corrosion current density as compared to CR iron (with similar OCP values). The corrosion rate of CR iron after 1 day (0.10 ± 0.01 mm/year) was comparable with the values found by others (0.17–0.24 mm/year) [51,52]. The corrosion rate of AM porous iron after 1 day was 1.18 mm/year, which is ≈12 times higher than that of CR iron and also higher than the values found for the iron samples fabricated using other techniques [53–55] and most of the iron alloys that have been studied so far [15]. This clearly shows the advantages of the refined microstructure from AM in increasing the biodegradation rate of slowly degrading metals such as iron. It is well known that microstructural features such as texture and dislocation density may affect the corrosion rate [51]. Particularly relevant here is that the decrease in grain size may contribute to passive film destabilisation [56]. The specific solidification process experienced during AM creates smaller grain sizes that in turn increase the grain boundary area with defects in the crystal structure and high internal energy [57]. Grain boundaries of large area are expected to be more chemically active in a corrosive medium [52,58].

The Bode impedance diagram showed that the changes of impedance had similar trends for AM and CR iron samples. The impedance modulus values at the low frequency range can provide information about the charge transfer resistance and separation processes at the metal surface of the corroding system and the impedance modulus value changes in the middle frequency range relate to resistive and capacitive evolutions of a layer on the surface of the substrate, e.g. by growth or (partial) dissolution of a cor-

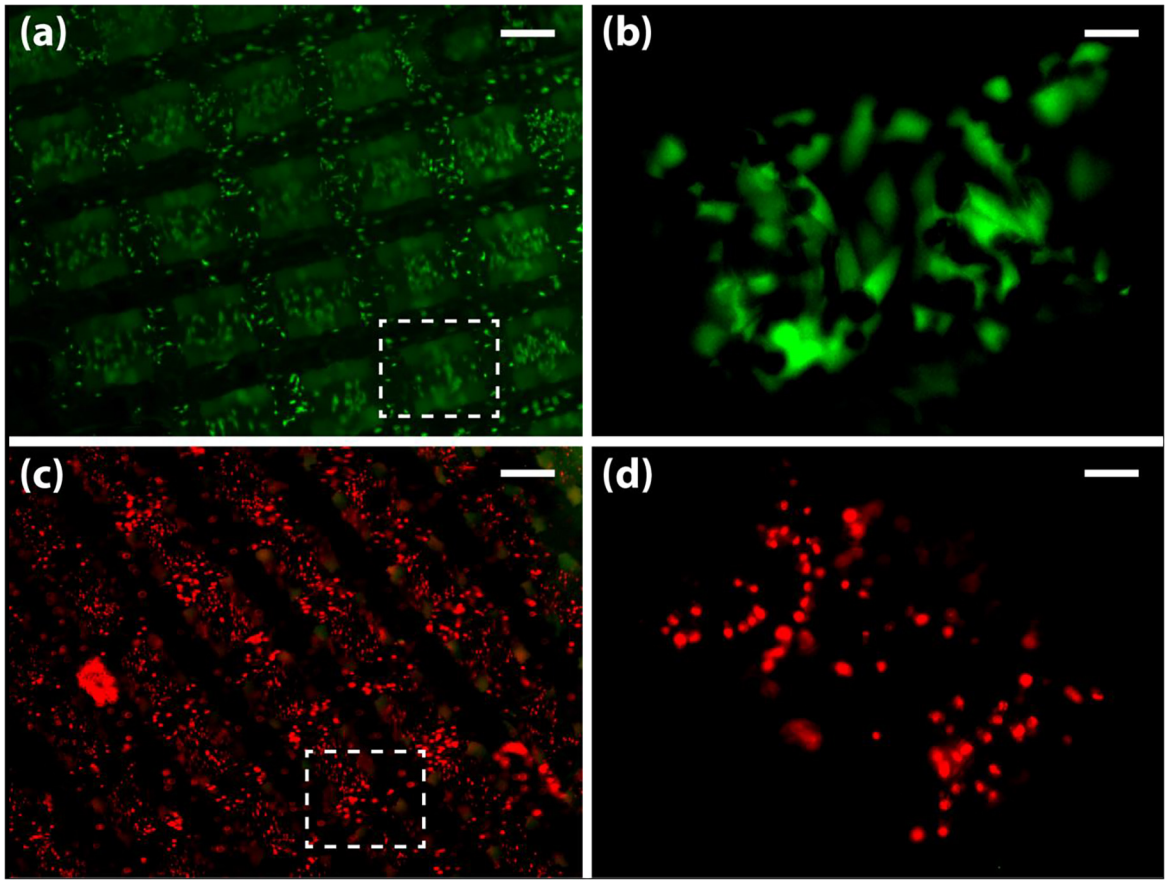

Fig. 7. Biocompatibility of AM iron scaffolds *in vitro*. MG-63 cells on Ti-6Al-4V (a, b) and iron (c, d) scaffolds, respectively. Low magnification fluorescent optical images (FOI) of cells attached to struts (a, c). Higher magnification of the boxed area of the lattice structure (b, d). Live cells, green; dead cells, red. Scale bars indicate 300 μm (a, c) and 30 μm (b, d). (For interpretation of the references to color in this figure legend, the reader is referred to the web version of this article.)

rosion product layer [59–61]. The increase of the impedance modulus at low frequency ($|Z|_{0.01Hz}$) from day 1 to day 3 relates to increasing corrosion resistance and could be attributed to the formation of a corrosion product layer at the beginning of the immersion test [46], also shown by the increasing impedance modulus values in the mid-frequency range ($|Z|_{10Hz}$). Then, the impedance modulus values at both low and mid frequency ranges decreased at day 7, probably resulting from relatively limited integrity and protectiveness of the corrosion product layer and hence increasing corrosion susceptibility of the underlying substrate. At the same immersion time points, AM iron samples always had lower impedance modulus values (or corrosion resistance) as compared to CR iron samples, which is in agreement with the results obtained from the PDP tests and further confirms the increased biodegradation rate of AM iron as compared to that of CR iron.

The immersion tests of the whole scaffolds showed a 3.1% weight reduction only after 28 days of immersion. If we normalize this with respect to a total theoretical surface area of 28 cm^2, the corrosion rate of the scaffolds is only 0.03 mm/year, which is one order of magnitude lower than the values reported by other researchers [51–53]. Visual inspection and SEM analysis suggested that there were different corrosion mechanisms operating from the periphery to the center of the scaffolds. At the periphery, degradation took place quite fast, as evidenced by the formation of a brownish layer after day 1 (Fig. 3a). In the center of the scaffolds, however, there were no brownish corrosion products even after 28 days. SEM revealed thinner, more adherent crystal-like corrosion products formed at the center of the samples with a thickness that increased with the immersion time (Fig. 4c, e). The degradation products were, however, loose and irregularly shaped on the periphery of the samples. EDS showed that the corrosion layer of external struts contained Ca and P elements (Fig. 4d, f), while no P element was found in the center of the scaffolds even after 28 days of immersion (Fig. 4e). Combined with ICP results (Fig. 3d), it was concluded that the Ca and P elements found on the corrosion layer came from r-SBF. To understand the different degradation mechanisms better, we inspected the surface morphology of the degraded struts after ultrasonic cleaning (Fig. 10). It was observed that r-SBF attacked the struts on the periphery of the samples and exposed the grains on their surfaces (Fig. 10a, b). The struts in the center of the samples, however, stayed almost intact (Fig. 10d). This explains why the normalized degradation rate is much smaller than the results reported in the literature. The local pH value is therefore expected to be different from the center to the periphery of the samples. In static immersion tests, scaffolds may have stagnant flow in the center and the diffusion of ions may be hampered. Gradually formed corrosion products on the outer surface of the scaffolds may further restrict the diffusion process. In addition, accumulation of OH^- ions in the center of the scaffolds may lead to the stabilization of the passive layer formed on the struts.

Another reason for the low weight loss measured here may be related to the limitations of the weight loss measurement and sample cleaning. For solid samples, weight loss measurement works quite well, because it is feasible to remove all the corrosion products with minimum attack to the sample itself. In the case of highly porous scaffolds, however, it is difficult to remove all the corrosion products, especially those in the center of the scaffolds. After cleaning, there were still corrosion products remaining not only in the

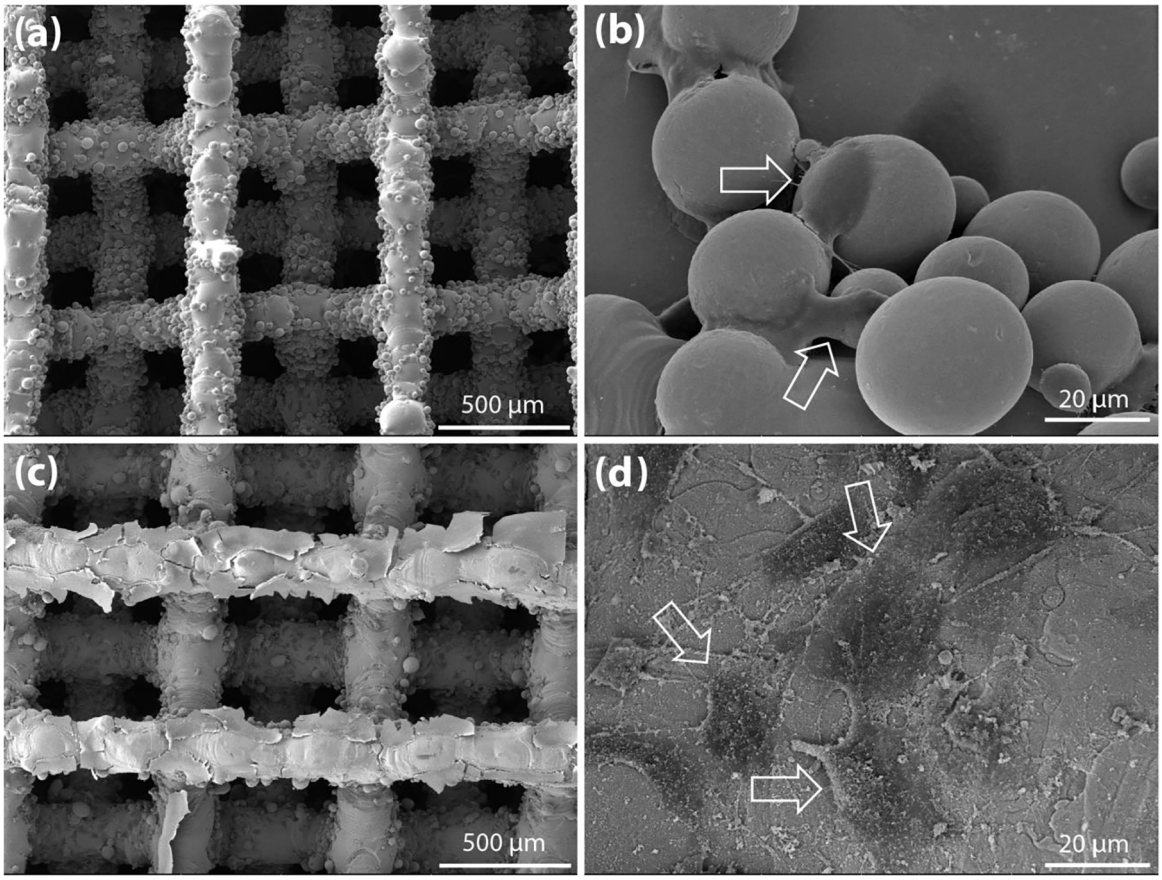

Fig. 8. Ultrastructural analyses of cell attachment *in vitro*. MG-63 cells on Ti-6Al-4V (a, b) and iron (c, d), respectively. Lower magnification scanning electron micrographs (SEM) of scaffold lattice structures (a, c) and higher magnifications (b, d) after seeding. Arrows indicate individual cells. Magnification indicated by scale bar.

center (Fig. 10d) but also on the periphery (Fig. 10c) of the scaffolds. The retained corrosion products on the periphery contained C, O, P, Ca and Fe (Fig. 10c, spot 001). In the center, the sphere-shaped corrosion products remained, which contained C, O, Fe and Ca (Fig. 10d. spot 1). As compared to the corrosion products before cleaning (Fig. 4e), the feather-like corrosion products could be removed, but the sphere-like structures still remained. Other researchers used acids or alkalis to remove the corrosion products [31,62–64], but this would cause extra deduction of the struts of the porous iron samples, especially on the periphery. ICP-OES analysis showed even less iron release to r-SBF as compared to the weight loss measurements, because iron ions participated in the formation of the corrosion products. That is why iron ion concentration even decreased after day 7.

Based on the reasoning above, it is clear that in addition to the microstructure and chemical composition, the topology of AM porous scaffolds greatly influences their degradation behavior. Optimizing the topological design of the porous structure could therefore be an effective measure for adjusting the degradation behavior of AM porous iron. For example, a larger pore size or a smaller diameter may further increase the degradation rate of iron scaffolds.

Moreover, the *in vitro* test environment affects the degradation rate as well. The inorganic ion concentrations in the immersion medium used here (r-SBF) are similar to the blood plasma. Hanks' solution [65] with higher Cl^- and lower HCO_3^- concentrations tends to increase the corrosion rate of iron. In addition, other researchers have reported higher degradation rates of iron in dynamic immersion tests [66]. Furthermore, without CO_2 control, the bulk pH of the medium keeps increasing, which could slow down the biodegradation. Follow-up studies in bioreactors and using other more complex biodegradation environments may alleviate some of these limitations. Finally, the degradation behavior of iron scaffolds needs to be evaluated *in vivo*. From the results obtained from earlier research [27], pure iron pin did not exhibit pronounced reduction in volume or mass in a rat model. Other researchers reported noticeable degradation of pure iron stents, while voluminous degradation products formed and remained even after longer implantation [32,67]. Peuster et al. [30] found that macrophages carrying iron contributed to the clearance of corrosion products from the implantation site as the solubility of iron degradation products in body fluid was low. Since a layer of corrosion products was also observed from our *in vitro* immersion tests, it would be of great interest to perform an *in vivo* study to compare additively manufactured iron scaffolds and solid iron in *in vivo* degradation behavior.

4.3. Mechanical behavior

The mechanical properties of the AM porous iron specimens remained within the ranges of the values of mechanical properties reported for trabecular bone (i.e., E = 500–20,000 MPa [68], σ_y = 0.2–80 MPa [69]) after 28 days of biodegradation. In the case of porous magnesium, which is reported to lose its structural integrity within a much shorter time, alloying or surface treatment is always needed [70–73]. In the case of porous iron, however, without any additional treatments or potentially toxic alloying elements, it has high mechanical properties, which is a distinct advantage.

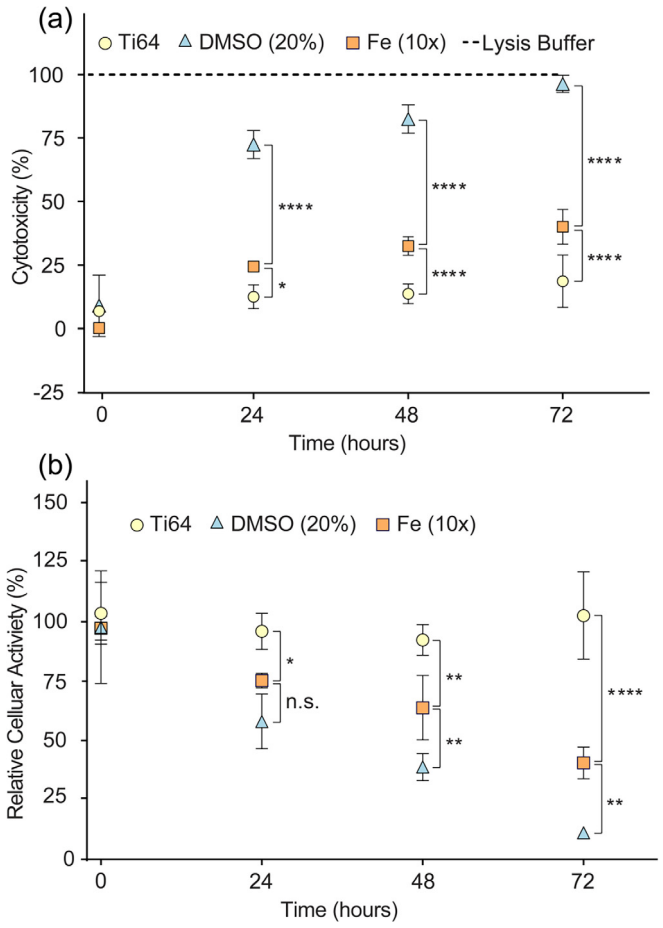

Fig. 9. Cytotoxicity *in vitro*. Relative cytotoxicity (a) and remaining cellular activity (b) of MG-63 cells upon exposure to AM iron scaffolds, as measured by LDH and MTS assay, respectively. Experiments were performed with extracts of randomly chosen replicate Fe-scaffolds (squares, n = 5) and compared to AM Ti-6Al-4V (balls, Ti64) scaffolds of the same design (n = 3). Dimethylsulfoxide (DMSO, triangles) and cell Lysis Buffer (dotted line, set to 100% in (a)) were used as controls. *n.s.*, not significant; *, $p < 0.05$; **, $p < 0.01$; ***, $p < 0.001$; ****, $p < 0.0001$.

Unlike other AM porous structures based on the diamond unit cell [74,75], the iron scaffolds studied here showed smooth stress-strain curves during uniaxial compression without fluctuations after the maximum stress. In addition, no sudden failure occurred and specimens still had a cylindrical shape at a strain of 60% (Fig. 6a inset). These could be explained by the high ductility of pure iron. Similar behaviors have been observed for other highly ductile porous materials, such as AM porous structures made from pure titanium and tantalum [9,11]. After *in vitro* immersion at given time points, it appeared that biodegradation has different influences on the stiffness from the yield strength of porous iron. It could be related to the different effects of interfacial bonding [76] (between the degradation products and iron) on the elastic modulus and yield strength of AM porous iron. Since the elastic modulus was measured over a narrow range of small strains, lateral dilation was insufficient to cause the interfacial separation and the load could still be carried by iron and its degradation products. As a result, accumulation of degradation products increased the elastic modulus of AM porous iron from day 2. After more corrosion occurred on the struts, despite increased amounts of degradation products, the elastic modulus of the scaffolds was also affected by the strut thickness. After 28 days of immersion, the elastic modulus of the specimens decreased to a value similar to that measured at day 1. This could be attributed to the trade-off between the reduction in the strut thickness and accumulation of corrosion products. For the yield strength of porous iron, the interfacial bonding became important. Load transfer at the interface between the degradation products and iron might be inefficient for poorly bonded degradation products, especially at strains close to the yield point. Then much of the load could not be carried by the degradation products and yield strength relied on the strength of the remained iron primarily. As a result, the strength of the degraded porous structure decreased, although in a small range, as the biodegradation process progressed.

4.4. Biological evaluation

In order to evaluate the potential of AM porous iron scaffolds for biomedical applications, we characterized their biocompatibility by using three different techniques: (i) a direct contact live-dead staining assay, (ii) visual inspection of attached cells in direct contact with the iron struts using electron micrographs, and (iii) two independent quantitative indirect cytotoxicity assays.

While SEM analyses (Fig. 8) showed polygonal shaped MG-63 cells in close contact with the iron surface (Fig. 8d; arrows, black) 24 h after seeding, in the magnified fluorescent images of the live-dead staining (Fig. 7) cells appeared to be more spherically condensed (Fig. 7d) on the iron surface as compared to more polygonal/spindle-shaped cells on Ti-6Al-4V (Fig. 7b) controls. Moreover, most cells appeared to be alive on Ti-6Al-4V but only a few on the iron surface from the dual channel images. Although classification of cell death remains challenging [77], from a morphological point of view, the observed condensation of MG-63 cells may be indicative of apoptosis, which is characterized by e.g., rounding-up, retraction of pseudopods, and a pyknotic cell volume reduction. The red fluorescence, on the other hand, is indicative of a loss of plasma membrane integrity and altogether hints towards a certain iron-mediated toxicity.

Although pure iron showed good biocompatibility during long time implantation as a biodegradable stent or pin [27,30,78,79], direct contact cytotoxicity was observed in several *in vitro* studies with different type of cells [80,81]. In contrast to the *in vitro* situation, released ions can be diluted *in vivo* and excreted from the local site into the body so that local concentrations will be diminished [32]. While *in vitro* cell seeding was conducted in a culture dish where released Fe ions can accumulate in a high concentration. The local Fe ion concentration on the surface of iron sample can be even higher. Furthermore, in our case, according to the former electrochemical tests, AM iron sample with fine grain structures are prone to rapider degradation and release a larger quantity of Fe ions. The higher Fe ion concentration can promote the formation of highly reactive oxygen species such as hydroxyl and superoxide radicals, which were highly toxic due to their rapid reaction ability with most molecules found in living cell [62]. In future studies, to better mimic the *in vivo* condition, bioreactor with dynamic and perfused environment should be applied to assess cytotoxicity.

We further employed two indirect contact assays to appreciate the influences of scaffold degradation products on cell metabolism: LDH and MTS assays. Compared to direct contact between AM iron scaffolds to MG-63 cells, the cytocompatibility according to ISO 10993 was reasonable in *in vitro* assays for up to 72 h. To better mimic the *in vivo* situation *in vitro*, we applied the latest recommended modification of EN ISO 10993-5 and 10993-12 and used a 10-times higher extraction ratio [82,83] for iron than the 0.2 g/mL that was used for Ti-6Al-4V. However, for our AM porous sample which has a larger surface area, 10-times dilution maybe still insufficient.

Besides Fe ion concentration, methodological differences or the used cell type may also play an important role for *in vitro* cytotoxicity study as shown by the contradictory results from literatures.

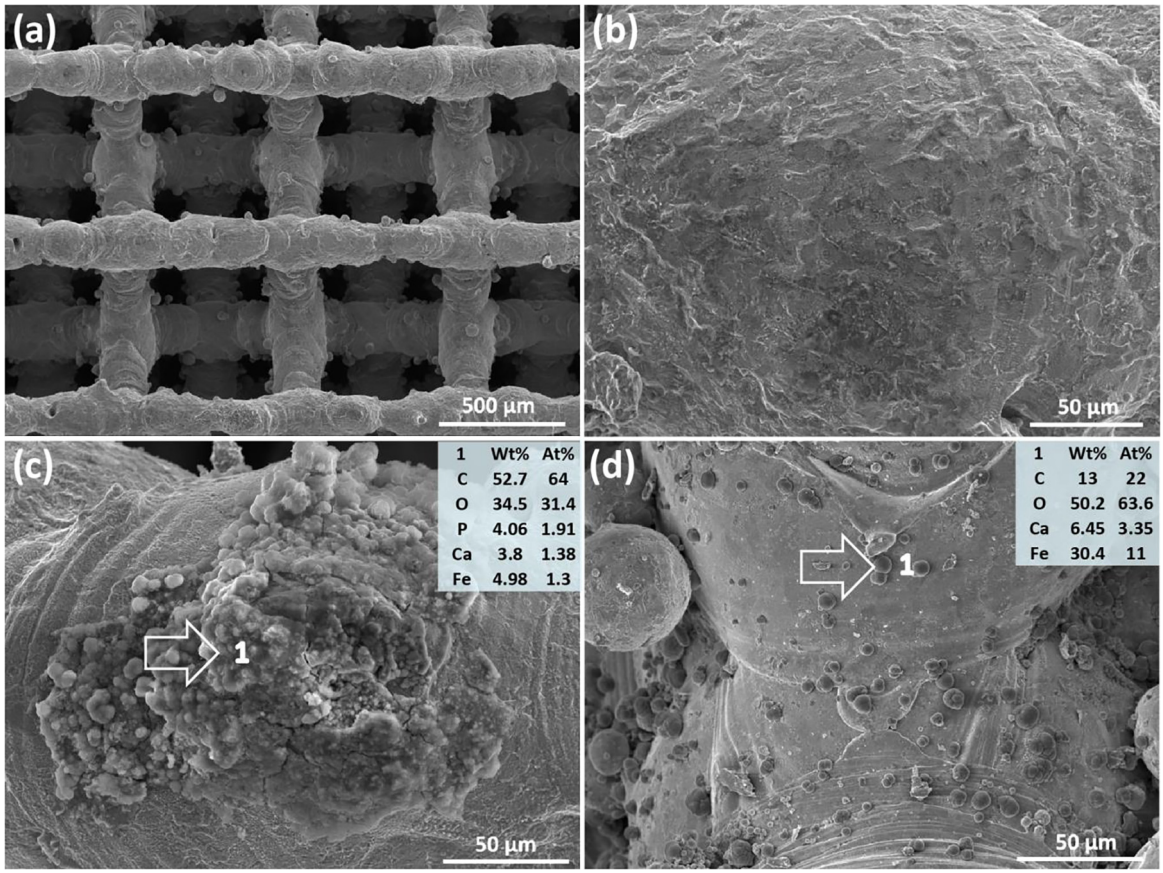

Fig. 10. SEM and EDS analyses of retained degradation products (28-day immersion) after cleaning: (a) strut morphology at a low magnification, (b) at a high magnification, (c) retained degradation products on the periphery and (d) in the center of the scaffolds. 1 indicates the spot where EDS analysis was performed.

Several other studies also used MG-63 to assess cytotoxicity of e.g., sandblasted 99.5% pure iron foils and observed that the "spreading behavior" of the cells was inhibited, showing a similar round-shape morphology [46]. While virtually all MG-63 cells on 'bare' iron revealed a green fluorescence even after 48 h, no live-dead ratio was calculated. A good *in vitro* cytocompatibility of 3D printed iron–manganese scaffolds, compared to tissue culture plastic, was earlier reported [29]. Interestingly, cell viability in MTT assays of undiluted short-term extracts was about 45% and surprisingly 80% in undiluted long-term extracts, using mouse calvaria-derived osteoblast-like MC3T3 cells, while live-dead staining in direct contact did not show any signs of physiological apoptosis even in supraconfluent 3-day cultures.

The typical iron concentration of mammalian cell culture media, like DMEM, is 0.25–3 M [84] and thus substantially lower than the average 23 M iron in plasma. Increasing iron content in culture media may also stimulate cell growth [84], as shown for mouse L-929 fibroblasts [85]. In contrast, toxic effects of iron are further abundantly reported: in a murine hepatocyte cell line just 25 M $FeSO_4$ induced 50% cell death within 3 h [84]. Interestingly, in neuroblastoma cells, 50% apoptosis occurred at 15 mM iron and none at 10 mM [86]. A diversity in the response to iron even between two different studies using the same cells reflects the idea that minor differences can lead to significant alterations in a cell's response to iron [84]. In addition, some contradictions in the literature may result from the differences in timing – although most studies used 24–48 h incubations [84]. Future studies should therefore apply ISO 10993 guidelines, providing sufficiently long time points (e.g., 24, 48, 72 h), disclose extraction ratios, and ideally use (more than one) relevant human indicator cells or cell lines. Finally, *in vivo* tests are required to investigate biodegradation and bone tissue response in terms of the iron-based orthopedic implant.

5. Conclusions

We demonstrated for the first time how DMP could be used to fabricate topologically ordered porous iron. The scaffolds presented a precisely controlled topology with fully interconnected pores. Over a period of 28 days of immersion tests, the elastic modulus and yield strength of the porous iron decreased insignificantly, i.e., 7% and 5%, respectively. The mechanical properties of porous iron remained within the values reported for trabecular bone even after 28 days of biodegradation. Electrochemical tests showed that the degradation rates of AM porous iron are up to ≈12 times higher than those of CR iron. During 28 days of immersion testing, the weight of the porous structures decreased by 3.1%. Different mechanisms were found to determine the biodegradation behavior on the periphery of the cylindrical scaffolds and in their center. This suggests that topological design plays an important role in adjusting the biodegradation behavior of AM porous iron. While direct contact between MG-63 cells and scaffolds revealed instant cytotoxicity in static cell culture, the cytocompatibility according to ISO 10993 was reasonable in *in vitro* assays for up to 72 h. Further systematic *in vitro* cytotoxicity study and *in vivo* implantation of the AM iron is necessary, a study that will be planned in the near future. Nevertheless, being the first reported study fabricating iron scaffolds through DMP, we believe that with appropriate design and bioactive coating [87], DMP porous Fe-based materials hold potential to become a new generation of functional and degradable biomaterials for orthopedic applications.

Acknowledgements

The research for this paper was financially supported by the Prosperos project, funded by the Interreg VA Flanders – The Netherlands program, CCI Grant No. 2014TC16RFCB04. Y.L. thanks the China Scholarship Council (CSC) for financial support. K.L. thanks VLAIO (Flanders Agency for Innovation and Entrepreneurship) for the financial support (IWT140257). A. Yilmaz and L. I. Fockaert acknowledge funding under project number F41.3.14546a and F81.6.13509 in the framework of the Partnership Program of the Materials Innovation Institute M2i (www.m2i.nl) and the Foundation of Fundamental Research on Matter (FOM) (www.fom.nl), which is part of the Netherlands Organisation for Scientific Research (www.nwo.nl). Ruud Hendrikx at the Department of Materials Science and Engineering of the Delft University of Technology is acknowledged for XRD analysis.

Appendix A. Supplementary data

Supplementary Figs. S1–S3 associated with this article can be found, in the online version, at https://doi.org/10.1016/j.actbio.2018.07.011.

References

[1] A.A. Zadpoor, J. Malda, Additive manufacturing of biomaterials, tissues, and organs, Ann. Biomed. Eng. 45 (2017) 1–11.
[2] L. Murr, S. Gaytan, F. Medina, H. Lopez, E. Martinez, B. Machado, D. Hernandez, L. Martinez, M. Lopez, R. Wicker, Next-generation biomedical implants using additive manufacturing of complex, cellular and functional mesh arrays, Philos. Trans. R. Soc. London A 368 (2010) 1999–2032.
[3] X. Wang, S. Xu, S. Zhou, W. Xu, M. Leary, P. Choong, M. Qian, M. Brandt, Y.M. Xie, Topological design and additive manufacturing of porous metals for bone scaffolds and orthopaedic implants: a review, Biomaterials 83 (2016) 127–141.
[4] A.A. Zadpoor, Mechanics of additively manufactured biomaterials, J. Mech. Behav. Biomed. Mater. 70 (2017) 1–6.
[5] A.H. Yusop, A.A. Bakir, N.A. Shaharom, M.R. Abdul Kadir, H. Hermawan, Porous biodegradable metals for hard tissue scaffolds: a review, Int. J. Biomater. 2012 (2012) 10.
[6] F.S.L. Bobbert, K. Lietaert, A.A. Eftekhari, B. Pouran, S.M. Ahmadi, H. Weinans, A. A. Zadpoor, Additively manufactured metallic porous biomaterials based on minimal surfaces: a unique combination of topological, mechanical, and mass transport properties, Acta Biomater. 53 (2017) 572–584.
[7] H.M. Kolken, S. Janbaz, S.M. Leeflang, K. Lietaert, H.H. Weinans, A.A. Zadpoor, Rationally designed meta-implants: a combination of auxetic and conventional meta-biomaterials, Mater. Horiz. 5 (2018) 28–35.
[8] S.M. Ahmadi, R. Hedayati, Y. Li, K. Lietaert, N. Tümer, A. Fatemi, C.D. Rans, B. Pouran, H. Weinans, A.A. Zadpoor, Fatigue performance of additively manufactured meta-biomaterials: the effects of topology and material type, Acta Biomater. 65 (2018) 292–304.
[9] R. Wauthle, S.M. Ahmadi, S. Amin Yavari, M. Mulier, A.A. Zadpoor, H. Weinans, J. Van Humbeeck, J.-P. Kruth, J. Schrooten, Revival of pure titanium for dynamically loaded porous implants using additive manufacturing, Mater. Sci. Eng., C 54 (2015) 94–100.
[10] C. Yan, L. Hao, A. Hussein, P. Young, D. Raymont, Advanced lightweight 316L stainless steel cellular lattice structures fabricated via selective laser melting, Mater. Des. 55 (2014) 533–541.
[11] R. Wauthle, J. van der Stok, S. Amin Yavari, J. Van Humbeeck, J.-P. Kruth, A.A. Zadpoor, H. Weinans, M. Mulier, J. Schrooten, Additively manufactured porous tantalum implants, Acta Biomater. 14 (2015) 217–225.
[12] S. Limmahakhun, A. Oloyede, K. Sitthiseripratip, Y. Xiao, C. Yan, Stiffness and strength tailoring of cobalt chromium graded cellular structures for stress-shielding reduction, Mater. Des. 114 (2017) 633–641.
[13] M. Moravej, D. Mantovani, Biodegradable metals for cardiovascular stent application: interests and new opportunities, Int. J. Mol. Sci. 12 (2011) 4250.
[14] S. Amin Yavari, J. van der Stok, Y.C. Chai, R. Wauthle, Z. Tahmasebi Birgani, P. Habibovic, M. Mulier, J. Schrooten, H. Weinans, A.A. Zadpoor, Bone regeneration performance of surface-treated porous titanium, Biomaterials 35 (2014) 6172–6181.
[15] Y.F. Zheng, X.N. Gu, F. Witte, Biodegradable metals, Mater. Sci. Eng.: R: Rep. 77 (2014) 1–34.
[16] D. Hong, D.-T. Chou, O.I. Velikokhatnyi, A. Roy, B. Lee, I. Swink, I. Issaev, H.A. Kuhn, P.N. Kumta, Binder-jetting 3D printing and alloy development of new biodegradable Fe-Mn-Ca/Mg alloys, Acta Biomater. 45 (2016) 375–386.
[17] N. Ikeo, R. Nakamura, K. Naka, T. Hashimoto, T. Yoshida, T. Urade, K. Fukushima, H. Yabuuchi, T. Fukumoto, Y. Ku, T. Mukai, Fabrication of a magnesium alloy with excellent ductility for biodegradable clips, Acta Biomater. 29 (2016) 468–476.
[18] X. Li, X. Liu, S. Wu, K.W.K. Yeung, Y. Zheng, P.K. Chu, Design of magnesium alloys with controllable degradation for biomedical implants: From bulk to surface, Acta Biomater. 45 (2016) 2–30.
[19] D. Zhao, S. Huang, F. Lu, B. Wang, L. Yang, L. Qin, K. Yang, Y. Li, W. Li, W. Wang, S. Tian, X. Zhang, W. Gao, Z. Wang, Y. Zhang, X. Xie, J. Wang, J. Li, Vascularized bone grafting fixed by biodegradable magnesium screw for treating osteonecrosis of the femoral head, Biomaterials 81 (2016) 84–92.
[20] D. Bian, W. Zhou, J. Deng, Y. Liu, W. Li, X. Chu, P. Xiu, H. Cai, Y. Kou, B. Jiang, Y. Zheng, Development of magnesium-based biodegradable metals with dietary trace element germanium as orthopaedic implant applications, Acta Biomater. 64 (2017) 421–436.
[21] Y. Liu, Y. Wu, D. Bian, S. Gao, S. Leeflang, H. Guo, Y. Zheng, J. Zhou, Study on the Mg-Li-Zn ternary alloy system with improved mechanical properties, good degradation performance and different responses to cells, Acta Biomater. 62 (2017) 418–433.
[22] J. Wang, Y. Wu, H. Li, Y. Liu, X. Bai, W. Chau, Y. Zheng, L. Qin, Magnesium alloy based interference screw developed for ACL reconstruction attenuates peri-tunnel bone loss in rabbits, Biomaterials 157 (2018) 86–97.
[23] H. Hermawan, Updates on the research and development of absorbable metals for biomedical applications, Progr. Biomater. (2018).
[24] A. Francis, Y. Yang, S. Virtanen, A.R. Boccaccini, Iron and iron-based alloys for temporary cardiovascular applications, J. Mater. Sci. – Mater. Med. 26 (2015) 1–16.
[25] J. He, F.-L. He, D.-W. Li, Y.-L. Liu, Y.-Y. Liu, Y.-J. Ye, D.-C. Yin, Advances in Fe-based biodegradable metallic materials, RSC Adv. 6 (2016) 112819–112838.
[26] Q. Peng, Y. Huang, L. Zhou, N. Hort, K.U. Kainer, Preparation and properties of high purity Mg–Y biomaterials, Biomaterials 31 (2010) 398–403.
[27] T. Kraus, F. Moszner, S. Fischerauer, M. Fiedler, E. Martinelli, J. Eichler, F. Witte, E. Willbold, M. Schinhammer, M. Meischel, P.J. Uggowitzer, J.F. Löffler, A. Weinberg, Biodegradable Fe-based alloys for use in osteosynthesis: outcome of an in vivo study after 52weeks, Acta Biomater. 10 (2014) 3346–3353.
[28] I.A.J. van Hengel, M. Riool, L.E. Fratila-Apachitei, J. Witte-Bouma, E. Farrell, A.A. Zadpoor, S.A.J. Zaat, I. Apachitei, Selective laser melting porous metallic implants with immobilized silver nanoparticles kill and prevent biofilm formation by methicillin-resistant Staphylococcus aureus, Biomaterials 140 (2017) 1–15.
[29] D.-T. Chou, D. Wells, D. Hong, B. Lee, H. Kuhn, P.N. Kumta, Novel processing of iron–manganese alloy-based biomaterials by inkjet 3-D printing, Acta Biomater. 9 (2013) 8593–8603.
[30] M. Peuster, C. Hesse, T. Schloo, C. Fink, P. Beerbaum, C. von Schnakenburg, Long-term biocompatibility of a corrodible peripheral iron stent in the porcine descending aorta, Biomaterials 27 (2006) 4955–4962.
[31] W. Lin, L. Qin, H. Qi, D. Zhang, G. Zhang, R. Gao, H. Qiu, Y. Xia, P. Cao, X. Wang, W. Zheng, Long-term in vivo corrosion behavior, biocompatibility and bioresorption mechanism of a bioresorbable nitrided iron scaffold, Acta Biomater. 54 (2017) 454–468.
[32] D. Andreas, H. Thomas, B.F. Wilhelm, P. Matthias, In vitro and in vivo corrosion properties of new iron–manganese alloys designed for cardiovascular applications, J. Biomed. Mater. Res. B Appl. Biomater. 103 (2015) 649–660.
[33] J. Čapek, D. Vojtěch, A. Oborná, Microstructural and mechanical properties of biodegradable iron foam prepared by powder metallurgy, Mater. Des. 83 (2015) 468–482.
[34] J. Farack, C. Wolf-Brandstetter, S. Glorius, B. Nies, G. Standke, P. Quadbeck, H. Worch, D. Scharnweber, The effect of perfusion culture on proliferation and differentiation of human mesenchymal stem cells on biocorrodible bone replacement material, Mater. Sci. Eng., B 176 (2011) 1767–1772.
[35] P. Quadbeck, R. Hauser, K. Kümmel, G. Standke, G. Stephani, B. Nies, S. Rößler, B. Wegener, Iron based cellular metals for degradable synthetic bone replacement. PM2010 World Congress, PM Biomaterials (2010) 1–8.
[36] Z. Wen, L. Zhang, C. Chen, Y. Liu, C. Wu, C. Dai, A construction of novel iron-foam-based calcium phosphate/chitosan coating biodegradable scaffold material, Mater. Sci. Eng., C 33 (2013) 1022–1031.
[37] N. Mohd Daud, N.B. Sing, A.H. Yusop, F.A. Abdul Majid, H. Hermawan, Degradation and in vitro cell–material interaction studies on hydroxyapatite-coated biodegradable porous iron for hard tissue scaffolds, J. Orthopaedic Transl. 2 (2014) 177–184.
[38] M. Heiden, E. Nauman, L. Stanciu, Bioresorbable Fe-Mn and Fe-Mn-HA materials for orthopedic implantation: enhancing degradation through porosity, Control. Adv Healthc. Mater. (2017;6.).
[39] R. Alavi, A. Trenggono, S. Champagne, H. Hermawan, Investigation on mechanical behavior of biodegradable iron foams under different compression test conditions, Metals 7 (2017) 202.
[40] Y. Su, S. Champagne, A. Trenggono, R. Tolouei, D. Mantovani, H. Hermawan, Development and characterization of silver containing calcium phosphate coatings on pure iron foam intended for bone scaffold applications, Mater. Des. 148 (2018) 124–134.
[41] A. Oyane, H.-M. Kim, T. Furuya, T. Kokubo, T. Miyazaki, T. Nakamura, Preparation and assessment of revised simulated body fluids, J. Biomed. Mater. Res. Part A 65A (2003) 188–195.
[42] Y. Li, J. Zhou, P. Pavanram, M.A. Leeflang, L.I. Fockaert, B. Pouran, N. Tümer, K.U. Schröder, J.M.C. Mol, H. Weinans, H. Jahr, A.A. Zadpoor, Additively manufactured biodegradable porous magnesium, Acta Biomater. 67 (2018) 378–392.
[43] T. Huang, J. Cheng, Y.F. Zheng, In vitro degradation and biocompatibility of Fe–Pd and Fe–Pt composites fabricated by spark plasma sintering, Mater. Sci. Eng., C 35 (2014) 43–53.

[44] A.H.M. Yusop, N.M. Daud, H. Nur, M.R.A. Kadir, H. Hermawan, Controlling the degradation kinetics of porous iron by poly (lactic-co-glycolic acid) infiltration for use as temporary medical implants, Sci. Rep. (2015;5.).
[45] A.C. Taş, P.J. Majewski, F. Aldinger, Chemical preparation of pure and strontium-and/or magnesium-doped lanthanum gallate powders, J. Am. Ceram. Soc. 83 (2000) 2954–2960.
[46] J. Zhou, Y. Yang, M. Alonso Frank, R. Detsch, A.R. Boccaccini, S. Virtanen, Accelerated,, Degradation behavior and cytocompatibility of pure iron treated with sandblasting, ACS Appl. Mater. Interfaces 8 (2016) 26482–26492.
[47] B. Song, X. Zhao, S. Li, C. Han, Q. Wei, S. Wen, J. Liu, Y. Shi, Differences in microstructure and properties between selective laser melting and traditional manufacturing for fabrication of metal parts: a review, Front. Mech. Eng. 10 (2015) 111–125.
[48] L.-E. Loh, C.-K. Chua, W.-Y. Yeong, J. Song, M. Mapar, S.-L. Sing, Z.-H. Liu, D.-Q. Zhang, Numerical investigation and an effective modelling on the Selective Laser Melting (SLM) process with aluminium alloy 6061, Int. J. Heat Mass Transf. 80 (2015) 288–300.
[49] A. Simchi, H. Pohl, Effects of laser sintering processing parameters on the microstructure and densification of iron powder, Mater. Sci. Eng., A 359 (2003) 119–128.
[50] B. Song, S. Dong, Q. Liu, H. Liao, C. Coddet, Vacuum heat treatment of iron parts produced by selective laser melting: microstructure, residual stress and tensile behavior, Mater. Des. (1980–2015) 54 (2014) 727–733.
[51] C.S. Obayi, R. Tolouei, C. Paternoster, S. Turgeon, B.A. Okorie, D.O. Obikwelu, G. Cassar, J. Buhagiar, D. Mantovani, Influence of cross-rolling on the microtexture and biodegradation of pure iron as biodegradable material for medical implants, Acta Biomater. 17 (2015) 68–77.
[52] C.S. Obayi, R. Tolouei, A. Mostavan, C. Paternoster, S. Turgeon, B.A. Okorie, D.O. Obikwelu, D. Mantovani, Effect of grain sizes on mechanical properties and biodegradation behavior of pure iron for cardiovascular stent application, Biomatter. 6 (2016) e959874.
[53] M. Moravej, A. Purnama, M. Fiset, J. Couet, D. Mantovani, Electroformed pure iron as a new biomaterial for degradable stents: In vitro degradation and preliminary cell viability studies, Acta Biomater. 6 (2010) 1843–1851.
[54] F.L. Nie, Y.F. Zheng, Surface chemistry of bulk nanocrystalline pure iron and electrochemistry study in gas-flow physiological saline, J. Biomed. Mater. Res. B Appl. Biomater. 100B (2012) 1404–1410.
[55] T. Jurgeleit, E. Quandt, C. Zamponi, Magnetron sputtering a new fabrication method of iron based biodegradable implant materials, Adv. Mater. Sci. Eng. 2015 (2015).
[56] K. Ralston, N. Birbilis, Effect of grain size on corrosion: a review, Corrosion 66 (2010). 075005-075005-075013.
[57] F. Witte, N. Hort, C. Vogt, S. Cohen, K.U. Kainer, R. Willumeit, F. Feyerabend, Degradable biomaterials based on magnesium corrosion, Curr. Opin. Solid State Mater. Sci. 12 (2008) 63–72.
[58] M. Moravej, S. Amira, F. Prima, A. Rahem, M. Fiset, D. Mantovani, Effect of electrodeposition current density on the microstructure and the degradation of electroformed iron for degradable stents, Mater. Sci. Eng., B 176 (2011) 1812–1822.
[59] C.V. Vidal, A.I. Muñoz, Electrochemical aspects in biomedical alloy characterization: electrochemical impedance spectroscopy, Biomed. Eng. Trends Mater. Sci.: InTech (2011).
[60] J. Tedim, M.L. Zheludkevich, A.C. Bastos, A.N. Salak, A.D. Lisenkov, M.G.S. Ferreira, Influence of preparation conditions of Layered Double Hydroxide conversion films on corrosion protection, Electrochim. Acta 117 (2014) 164–171.
[61] B. Van der Linden, H. Terryn, J. Vereecken, Investigation of anodic aluminium oxide layers by electrochemical impedance spectroscopy, J. Appl. Electrochem. 20 (1990) 798–803.
[62] E. Zhang, H. Chen, F. Shen, Biocorrosion properties and blood and cell compatibility of pure iron as a biodegradable biomaterial, J. Mater. Sci. – Mater. Med. 21 (2010) 2151–2163.
[63] J. Čapek, Š. Msallamová, E. Jablonská, J. Lipov, D. Vojtěch, A novel high-strength and highly corrosive biodegradable Fe-Pd alloy: structural, mechanical and in vitro corrosion and cytotoxicity study, Mater. Sci. Eng., C 79 (2017) 550–562.
[64] P. Mariot, M.A. Leeflang, L. Schaeffer, J. Zhou, An investigation on the properties of injection-molded pure iron potentially for biodegradable stent application, Powder Technol. 294 (2016) 226–235.
[65] H. Hermawan, D. Dubé, D. Mantovani, Degradable metallic biomaterials: Design and development of Fe–Mn alloys for stents, J. Biomed. Mater. Res. Part A 93A (2010) 1–11.
[66] B. Liu, Y.F. Zheng, Effects of alloying elements (Mn Co, Al, W, Sn, B, C and S) on biodegradability and in vitro biocompatibility of pure iron, Acta Biomater. 7 (2011) 1407–1420.
[67] D. Pierson, J. Edick, A. Tauscher, E. Pokorney, P. Bowen, J. Gelbaugh, J. Stinson, H. Getty, C.H. Lee, J. Drelich, J. Goldman, A simplified in vivo approach for evaluating the bioabsorbable behavior of candidate stent materials, J. Biomed. Mater. Res. B Appl. Biomater. 100B (2012) 58–67.
[68] J. Parthasarathy, B. Starly, S. Raman, A. Christensen, Mechanical evaluation of porous titanium (Ti6Al4V) structures with electron beam melting (EBM), J. Mech. Behav. Biomed. Mater. 3 (2010) 249–259.
[69] M. Yazdimamaghani, M. Razavi, D. Vashaee, K. Moharamzadeh, A.R. Boccaccini, L. Tayebi, Porous magnesium-based scaffolds for tissue engineering, Mater. Sci. Eng., C 71 (2017) 1253–1266.
[70] M.E. Iskandar, A. Aslani, H. Liu, The effects of nanostructured hydroxyapatite coating on the biodegradation and cytocompatibility of magnesium implants, J. Biomed. Mater. Res. Part A 101A (2013) 2340–2354.
[71] M. Yazdimamaghani, M. Razavi, D. Vashaee, V.R. Pothineni, J. Rajadas, L. Tayebi, Significant degradability enhancement in multilayer coating of polycaprolactone-bioactive glass/gelatin-bioactive glass on magnesium scaffold for tissue engineering applications, Appl. Surf. Sci. 338 (2015) 137–145.
[72] M. Yazdimamaghani, M. Razavi, D. Vashaee, L. Tayebi, Surface modification of biodegradable porous Mg bone scaffold using polycaprolactone/bioactive glass composite, Mater. Sci. Eng., C 49 (2015) 436–444.
[73] M. Razavi, M. Fathi, O. Savabi, D. Vashaee, L. Tayebi, Improvement of biodegradability, bioactivity, mechanical integrity and cytocompatibility behavior of biodegradable Mg based orthopedic implants using nanostructured bredigite (Ca7MgSi4O16) bioceramic coated via ASD/EPD technique, Ann. Biomed. Eng. 42 (2014) 2537–2550.
[74] S. Ahmadi, S. Yavari, R. Wauthle, B. Pouran, J. Schrooten, H. Weinans, A. Zadpoor, Additively manufactured open-cell porous biomaterials made from six different space-filling unit cells: the mechanical and morphological properties, Materials 8 (2015) 1871.
[75] R. Hedayati, S.M. Ahmadi, K. Lietaert, B. Pouran, Y. Li, H. Weinans, C.D. Rans, A. A. Zadpoor, Isolated and modulated effects of topology and material type on the mechanical properties of additively manufactured porous biomaterials, J. Mech. Behav. Biomed. Mater. 79 (2018) 254–263.
[76] S.-Y. Fu, X.-Q. Feng, B. Lauke, Y.-W. Mai, Effects of particle size, particle/matrix interface adhesion and particle loading on mechanical properties of particulate–polymer composites, Compos. B Eng. 39 (2008) 933–961.
[77] G. Kroemer, W.S. El-Deiry, P. Golstein, M.E. Peter, D. Vaux, P. Vandenabeele, B. Zhivotovsky, M.V. Blagosklonny, W. Malorni, R.A. Knight, M. Piacentini, S. Nagata, G. Melino, Classification of cell death: recommendations of the Nomenclature Committee on Cell Death, Cell Death Diff. 12 (2005) 1463.
[78] A. Francis, Y. Yang, S. Virtanen, A.R. Boccaccini, Iron and iron-based alloys for temporary cardiovascular applications, J. Mater. Sci. – Mater. Med. 26 (2015) 138.
[79] M. Peuster, P. Wohlsein, M. Brügmann, M. Ehlerding, K. Seidler, C. Fink, H. Brauer, A. Fischer, G. Hausdorf, A novel approach to temporary stenting: degradable cardiovascular stents produced from corrodible metal—results 6–18 months after implantation into New Zealand white rabbits, Heart 86 (2001) 563–569.
[80] C. Yang, Z. Huan, X. Wang, C. Wu, J. Chang, 3D printed Fe scaffolds with HA nanocoating for bone regeneration, ACS Biomater. Sci. Eng. 4 (2018) 608–616.
[81] R. Oriňáková, A. Oriňák, L.M. Bučková, M. Giretová, Ľ. Medvecký, E. Labbanczová, M. Kupková, M. Hrubovčáková, K. Koval', Iron based degradable foam structures for potential orthopedic applications, Int. J. Electrochem. Sci. 8 (2013) 12451–12465.
[82] J. Fischer, D. Pröfrock, N. Hort, R. Willumeit, F. Feyerabend, Reprint of: Improved cytotoxicity testing of magnesium materials, Mater. Sci. Eng., B 176 (2011) 1773–1777.
[83] J. Wang, F. Witte, T. Xi, Y. Zheng, K. Yang, Y. Yang, D. Zhao, J. Meng, Y. Li, W. Li, K. Chan, L. Qin, Recommendation for modifying current cytotoxicity testing standards for biodegradable magnesium-based materials, Acta Biomater. 21 (2015) 237–249.
[84] R. Eid, N.T.T. Arab, M.T. Greenwood, Iron mediated toxicity and programmed cell death: a review and a re-examination of existing paradigms, Biochim. Biophys. Acta (BBA) – Molecular Cell Res. (1864, 2017,) 399–430.
[85] R.R. Zombola, R.C. Bearse, P.A. Kitos, Trace element uptake by L-cells as a function of trace elements in a synthetic growth medium, J. Cell. Physiol. 101 (1979) 57–65.
[86] K.C. Chew, E.-T. Ang, Y.K. Tai, F. Tsang, S.Q. Lo, E. Ong, W.-Y. Ong, H.-M. Shen, K.-L. Lim, V.L. Dawson, Enhanced autophagy from chronic toxicity of iron and mutant A53T α-synuclein implications for neuronal cell death in Parkinson disease, J. Biol. Chem. 286 (2011) 33380–33389.
[87] S. Ray, U. Thormann, M. Eichelroth, M. Budak, C. Biehl, M. Rupp, U. Sommer, T. El Khassawna, F.I. Alagboso, M. Kampschulte, M. Rohnke, A. Henß, K. Peppler, V. Linke, P. Quadbeck, A. Voigt, F. Stenger, D. Karl, R. Schnettler, C. Heiss, K.S. Lips, V. Alt, Strontium and bisphosphonate coated iron foam scaffolds for osteoporotic fracture defect healing, Biomaterials 157 (2018) 1–16.